


## Article

# SRTM DEM Correction Based on PSO-DBN Model in Vegetated Mountain Areas

Xinpeng Sun <sup>1</sup>, Cui Zhou <sup>1,\*</sup>, Jian Xie <sup>2</sup>, Zidu Ouyang <sup>1</sup> and Yongfeng Luo <sup>1</sup> 

<sup>1</sup> College of Science, Central South University of Forestry and Technology, Changsha 410004, China; xpsun@csuft.edu.cn (X.S.); 20200046@csuft.edu.cn (Z.O.); yfluo@csuft.edu.cn (Y.L.)

<sup>2</sup> School of Earth Science and Spatial Information Engineering, Hunan University of Science and Technology, Xiangtan 411201, China; xiejian@hnust.edu.cn

\* Correspondence: cuizhou@csuft.edu.cn

**Abstract:** The Shuttle Radar Topography Mission (SRTM) digital elevation model (DEM) is extensively utilized in various fields, such as forestry, oceanography, geology, and hydrology. However, due to limitations in radar side-view imaging, the SRTM DEM still contains gaps and anomalies, particularly in areas with an intricate topography, like forests. To enhance the accuracy of the SRTM DEM in forested regions, commonly employed approaches include regression analysis and artificial neural networks (ANN). Nevertheless, existing regression methods struggle to accurately capture the intricate nonlinear relationship between the error and influencing factors. Additionally, traditional ANN models are susceptible to overfitting, resulting in subpar accuracy. Deep Belief Network (DBN) is a highly precise algorithm in deep learning. However, the intricate combination of hyperparameters often leads to limited generalization ability and model robustness when correcting DEM. The present study proposes an error prediction model based on the DBN optimized by Particle Swarm Optimization (PSO) for SRTM DEM correction. By utilizing the PSO algorithm, we aim to identify the optimal combination of hyperparameters of DBN, including the number of neurons in the hidden layer and the learning rates. The experiment focuses on two regions in Hunan Province, China, characterized by abundant vegetation cover. The reference data utilized for comparison is ICESat/GLAS data. The experimental results demonstrate that the mean error (ME) and root mean square error (RMSE) of the SRTM DEM corrected by the proposed algorithm in these two regions are significantly reduced by 93.5%–96.0% and 21.5%–23.5%, respectively. Moreover, there is an improvement of over 26.1% in accuracy within complex terrain areas. Specifically, in broadleaf forest, the PSO-DBN method exhibits a remarkable accuracy improvement of 26.2%, while the DBN-corrected SRTM DEM shows an improvement of 15.3%. In coniferous forest, the PSO-DBN method achieves an accuracy improvement of 14.8%, whereas the DBN-corrected SRTM DEM demonstrates a gain of 5.8%. The approach provides a more effective and robust tool for correcting SRTM DEM or other similar DEMs over vegetated mountain areas.



**Citation:** Sun, X.; Zhou, C.; Xie, J.; Ouyang, Z.; Luo, Y. SRTM DEM Correction Based on PSO-DBN Model in Vegetated Mountain Areas. *Forests* **2023**, *14*, 1985. <https://doi.org/10.3390/f14101985>

Academic Editor: Giorgos Mallinis

Received: 26 August 2023

Revised: 27 September 2023

Accepted: 29 September 2023

Published: 1 October 2023

**Keywords:** digital elevation model; SRTM DEM; ICESat-2; forest; PSO-DBN



**Copyright:** © 2023 by the authors. Licensee MDPI, Basel, Switzerland. This article is an open access article distributed under the terms and conditions of the Creative Commons Attribution (CC BY) license (<https://creativecommons.org/licenses/by/4.0/>).

## 1. Introduction

The Digital Elevation Model (DEM) is a widely utilized mathematical model in the fields of Geographic Information Systems (GIS) and Remote Sensing (RS), serving as a crucial data source for various applications, such as topographic surveys [1], hydrological simulation [2], forest resource management [3], and disaster assessment [4]. There are three primary methods for acquiring DEM products, with the first method involving the utilization of optical sensors that capture data from instruments like the Advanced Spaceborne Thermal Emission and Reflection Radiometer (ASTER) DEM [5] and Advanced Land Observing Satellite (ALOS) World 3D—30 m (AW3D30) DEM [6]. These DEMs provide an accurate representation of steep slopes due to the nadir view of the sensor.

However, they are susceptible to interference from factors such as cloud cover, mist, and lack of texture [7]. The second method for acquiring DEM products is through Interferometric Synthetic Aperture Radar (InSAR). InSAR DEMs have the advantage of being all-weather capable, having high penetration capability, high accuracy, and fast speed. However, they are still influenced by gaps and anomalies due to the limitations of the radar's side view imaging modes. Examples of InSAR DEMs include SRTM (Shuttle Radar Topography Mission) DEM [8], TerraSAR-X add-on for Digital Elevation Measurement (TanDEM-X DEM) [9], and Copernicus DEM [10]. The third method involves acquiring data through airborne light detection and ranging (LiDAR), typically mounted on unmanned aerial vehicles (UAVs) or planes. DEMs generated using LiDAR technology generally exhibit higher vertical accuracy and spatial resolution compared to other sources, with a vertical accuracy ranging from 0.05 m to 0.15 m and horizontal point spacing typically ranging from 1 m to 3 m [11]. Therefore, LiDAR-based DEMs can be used as reference data to correct satellite-based DEMs [12,13]. However, LiDAR-based DEMs are associated with a high cost [14], which limits their widespread use for large-scale terrain data.

The SRTM DEM is the first globally available high-spatial resolution DEM product, and is widely recognized for its availability, accuracy, timeliness, and coverage [15–18]. However, it exhibits limitations in forested areas due to factors such as radar side-view imaging and band penetration, leading to significant vertical errors and reduced precision [19]. The enhancement of vertical accuracy in SRTM DEM within vegetated areas is crucial for applications such as forest tree height calculation, forest biomass estimation, and forest carbon stock monitoring. In recent years, the fusion of multi-source elevation data has emerged as a popular approach to rectify errors in SRTM DEM. These fusion methods can be classified into two categories: surface–surface data fusion model and point–surface data fusion model, depending on the type of elevation data integrated. The surface–surface data fusion model involves the integration of SRTM DEM with multiple high-precision DEMs. For instance, Wendi et al. utilized high-precision DEM data with a vertical resolution of 1 m and employed a Feedforward Neural Network (FNN) to establish a training model for the purpose of rectifying the SRTM DEM [20]. The fusion technique involving ASTER DEM and SRTM DEM data is employed as an approach to enhance the accuracy of mountainous terrain in cases where reference data is unavailable [21]. However, this surface–surface data fusion method necessitates expensive and limited high-precision DEM control data as a reference, which restricts its applicability for large-scale error correction. On the other hand, point–surface data fusion involves integrating precise elevation control point data with SRTM DEM information, thereby enhancing the precision of the SRTM DEM. One commonly employed approach involves establishing a regression model that correlates influencing factors, such as vegetation and topography, with the errors in SRTM DEM [12,22–24]. However, these models are limited to fitting specific functions and fail to accurately capture the nonlinear relationship between the influencing factors and the errors. Another strategy is to leverage machine learning algorithms for correcting SRTM DEM. For instance, integrating multiple machine learning algorithms can enhance the accuracy of SRTM DEMs [25]. In forested areas, one method for correcting the SRTM DEM involves subtracting the simulated forest height obtained through Random Forest (RF) from the original SRTM DEM [26].

Currently, artificial neural networks, being the predominant algorithm in machine learning, have been extensively applied to enhance SRTM DEMs within forested regions. Li, et al. [27] in their study proposed a method for rectifying forest DEMs using the back-propagation neural network (BPNN). This approach considers elevation spatial auto-correlation and mitigates vegetation bias (VB) present in DEMs across different types of forests. However, it is worth noting that the utilization of ANN algorithms may sometimes face challenges, such as gradient vanishing or explosion, resulting in models with reduced robustness and limited generalization capabilities. The Deep Belief Network (DBN) is a deep neural network architecture that consists of multiple layers of Restricted Boltzmann Machines (RBM). It possesses the capability to initialize the weight parameters of

the network using a unsupervised layer-wise pre-training approach. This initialization method serves the purpose of addressing issues related to gradient vanishing or explosion, which can occur due to random initialization [28]. For instance, Yue L. [29] proposed a point–surface fusion model based on DBN that addressing terrain slope, ground cover, and spatial location information to account for their effects on DEM elevation errors. Here, this study proposes a DEM error correction model, which effectively enhances data accuracy and addresses challenges such as data nulls, noise, and outliers. However, it is important to acknowledge that the DBN model’s performance is significantly influenced by its parameters. Inappropriate network parameter settings may lead to learning convergence towards a locally optimal solution. Additionally, the manual configuration of the number of layers and nodes in a DBN often gives rise to issues like model overfitting. Therefore, this paper presents a Particle Swarm Optimized Deep Confidence Network (PSO-DBN) for correcting SRTM DEM. The proposed method utilizes ICESat-2 ATL08 as the reference dataset and optimizes the hyperparameter combination of the deep confidence network using particle swarm optimization algorithm. This approach not only avoids local optima but also effectively addresses the complexity and variability inherent in SRTM DEM errors within forested regions. The effectiveness of the algorithm is validated in two experimental areas with diverse and complex terrain and vegetation conditions in Hunan Province, China.

This paper is structured as follows: Section 2 provides a comprehensive description of the study area, data sources, and processing methods; Section 3 elucidates the principles and steps involved in the PSO-DBN error correction model; Section 4 showcases the experimental results and conducts thorough analyses; finally, Section 5 presents conclusive remarks and future prospects.

## 2. Study Areas and Data

### 2.1. Study Areas

In this study, Chenzhou and Yongzhou, located in southern part of Hunan Province, China, were selected as the study area (Figure 1). Yongzhou (Figure 1c,e and Table 1) is situated at the confluence of the second and third terraces in southern Hunan Province. It covers a land area of 22,259 km<sup>2</sup> and exhibits diverse and intricate geomorphology. Bounded by mountains on three sides, Yongzhou features mountainous basins and valleys, with varying elevations across different regions. The elevation ranges from 45 m to 1992 m above sea level, with higher elevations found in the southwest and lower elevations in the northeast and central areas. The terrain predominantly consists of mountains, which account for over 70% of the total area. On average, these mountains have an elevation of 434.3 m with a slope gradient averaging at 15.3°. Forest cover measures approximately at 61.9%, while trees reach an average height of 7.5 m.

**Table 1.** Characteristics of the study area in Yongzhou and Chenzhou, including area, elevation, slope, canopy height, and vegetation cover.

Region	Area (km <sup>2</sup> )	Mean Elevation (m)	Mean Slope (°)	Mean Canopy Height (m)	Vegetation Coverage (%)
Yongzhou	22259	434.3	15.3	7.5	61.9
Chenzhou	19387	493.3	15.7	8.1	67.7

Chenzhou (Figure 1d,f and Table 1) is located in the southeastern region of Hunan Province, encompassing a land area of 19,387 km<sup>2</sup>. Its elevation ranges from 42 m and 2034 m, with an average elevation of 493.3 m and an average slope gradient of 15.7°. The topography descends from the southeast to the northwest, featuring prominent mountain ranges in the eastern and southern directions, while the northern and western areas consist of basin terrain with relatively low relief. The region showcases a rich array of vegetation, encompassing forests, shrublands, meadows, and wetlands. Notably, it has a forest cover-

age rate of 67.7%, with an average tree height of 8.1 m, establishing itself as one of Hunan Province's most abundant areas in terms of forest resources.

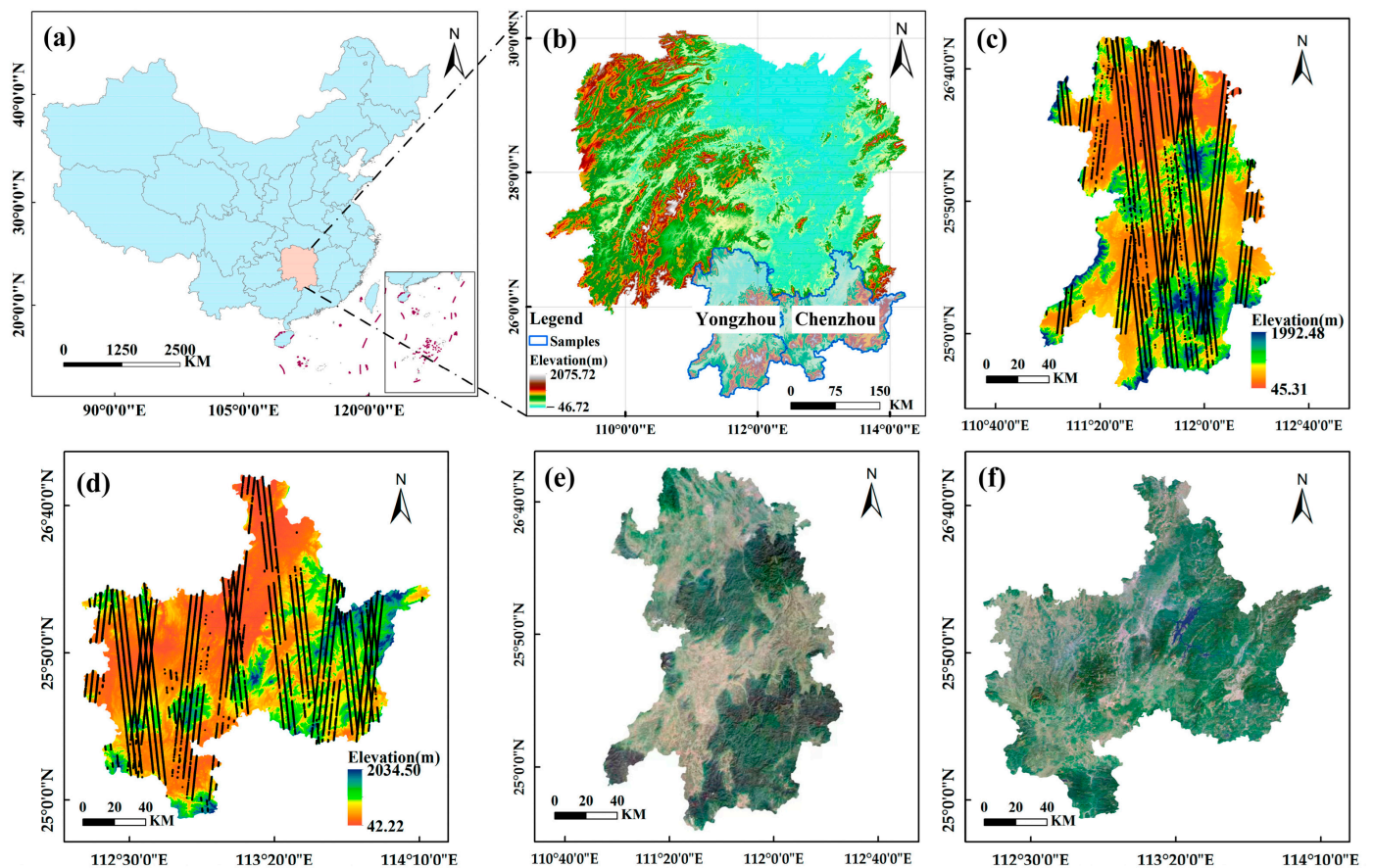


**Figure 1.** Location (a) and terrain data (b) of Hunan province, China. Terrains of Yongzhou and Chenzhou regions are shown in (c,d). Landsat-8 satellite image of Yongzhou and Chenzhou are shown in (e,f). Blue lines in (b) indicate the two selected regions. The black circles in (c,d) mark the locations of used ICESat-2 points.

## 2.2. SRTM DEM

The Shuttle Radar Topography Mission (SRTM) was conducted by the U.S. Space Shuttle Endeavour in 2000, utilizing radar mapping technology to acquire precise topographic data. This comprehensive mission covered approximately 80% of the Earth's land surface, spanning from 60° N to 56° S latitudes. The SRTM effectively employed radar in both the X and C-bands, employing synthetic aperture radar (SAR) interferometry techniques [30] to generate a high-resolution DEM. The horizontal datum of the SRTM DEM is based on the World Geodetic System 1984 (WGS-84), while the vertical datum is established using the mean sea level as determined by the WGS-84 Earth Gravity Model geoid. The data has been designed to achieve a planimetric accuracy within  $\pm 20$  m and an elevation accuracy within  $\pm 16$  m [31,32]. The third version of the SRTM DEM (SRTM NASA Version 3) with a horizontal resolution of 30 m was chosen for this study. To address any data gaps, additional information from the ASTER GDEM and USGS GMTED2010 elevation datasets were incorporated into the SRTM NASA Version 3. These datasets can be downloaded from the USGS Earth Explorer website (<https://earthexplorer.usgs.gov/>) (accessed on 26 October 2022).



### 2.3. ICESat-2

The Ice, Cloud, and Land Elevation Satellite-2 (ICESat-2) represents the latest advancement in global laser altimetry satellite technology, and was launched in September 2018. Equipped with the Advanced Terrain Laser Altimetry System (ATLAS), ICESat-2 is designed to measure surface reflections of laser beams and calculate the time taken for reflection in order to determine Earth's surface elevation [33]. The ICESat-2 mission provides distinct product categories for different surfaces, including ATL06 (land ice), ATL07 (sea ice), ATL08 (land/vegetation), ATL09 (atmosphere), ATL12 (oceans), and ATL13 (inland water). For the purposes of this study, we utilized the 2019–2022 ICESat-2 ATL08 dataset as the reference data source, which can be accessed through the website (<https://search.earthdata.nasa.gov>) (accessed on 29 October 2022). Any absolute assessment of vertical accuracy necessitates precise and independent reference data [19,34], with the accuracy of reference data being at least three times that of the evaluated DEM [35]. ATL08 demonstrates a vertical error of 0.2 m in plain terrains and 2 m in mountainous regions [36]. To ensure consistency between the reference data and SRTM DEM in terms of planimetric and elevation datums, a multi-step process was followed. Initially, elevation points with an absolute error exceeding 50 m between the SRTM DEM and elevation control points were excluded [37]. The laser point attribute information contained within the SRTM DEM dataset was subsequently utilized to enhance the screening process, resulting in the elimination of voids and outliers associated with topography, vegetation cover, and other factors. Ultimately, this refinement process led to the selection of 48,319 and 45,583 ICESat-2 data points in the Chenzhou and Yongzhou regions, respectively.

### 2.4. Ancillary Data

This study was conducted utilizing the Google Earth Engine (GEE) platform, which enables direct access to Landsat-8 source data. The dataset underwent a series of processing steps, including cloud removal, computational analysis, and spatial cropping. As a result, a Landsat-NDVI dataset with a horizontal resolution of 250 m was generated within the designated study area. Subsequently, the NDVI data achieved a 30 m resolution through the utilization of the nearest neighbor sampling method [38]. The data can be obtained from (<https://earthexplorer.usgs.gov/>) (accessed on 12 November 2022).

Previous research has established that the accuracy of SRTM DEM data is intricately linked to land use types, topographic factors, and vegetation cover types [39–41]. Therefore, this study incorporated GlobeLand30, a 2019 global surface fine cover dataset with a spatial resolution of 30 m obtained from (<http://www.globallandcover.com>) (accessed on 1 November 2022). Additionally, the global 30 m ground cover fine classification product (GLC\_FCS30) was employed to further categorize distinct vegetation types within forested areas, including differentiating dominant tree species, such as broadleaf forests and needle-leaved forests. Considering previous experiments that have demonstrated the significant impact of topographic factors on SRTM DEM elevation errors [42–44], this study incorporates slope and slope direction as crucial model input parameters.

## 3. Methodology

This study introduces a PSO-DBN model specifically designed to rectify errors in SRTM DEM data within forested regions, with a focus on its application and testing in the forests of Hunan Province, China. The PSO algorithm, classified as a Smart Swarm Optimization algorithm, is employed to search for global optimal solutions by simulating particle movements within a population. Within the PSO-DBN algorithm, the PSO algorithm plays a crucial role in identifying the optimal combination of hyperparameters for the DBN model, including factors such as the number of neurons in the hidden layer and the learning rate. The implementation process of this methodology primarily consists of four key components: training the DBN network structure, optimizing DBN hyperparameters using PSO, correcting forested SRTM DEM data through the PSO-DBN algorithm, and subsequently evaluating accuracy of the corrected SRTM DEM.

Following preprocessing of experimental data, the training phase for the DBN network structure commenced. The input data for this phase included six factors associated with terrain and vegetation: longitude, latitude, slope, slope direction, Normalized Difference Vegetation Index (NDVI), as well as land cover type. These factors also form part of the input layer within DBN. The output layer comprises elevation error values obtained from ICESat-2 ATL08 dataset along with SRTM DEM. The training process involved two primary stages: greedy pre-training and comprehensive fine-tuning. Initially following an approach described in Ref. [29], we established two Restricted Boltzmann Machine (RBM) network structures, as illustrated in Figure 2. Each RBM consists of a visible layer (first-layer) alongside a hidden one (second-layer), enabling unsupervised learning and feature extraction. Multiple sets of RBMs were utilized to optimize node weights through a layer-by-layer greedy pre-training BPNN technique. In this process, input data was fed into the visible layer, generating a vector  $v$ . This vector then underwent weight calculations  $w_1$ , resulting in values for the hidden layer  $H_1$ . Subsequently, using the hidden layer  $H_1$  of the current layer as input, backpropagation is performed to update the weight  $w_1$  between the hidden layer  $H_1$  and the visible layer  $v$ , and then the hidden layer  $H_1$  of  $RBM_1$  is used as the visible layer of the next layer  $RBM_2$ . This iterative process continued until all layers underwent pre-training. A comprehensive fine-tuning phase followed in a forward sequential manner, starting from the BP layer. Here, supervised learning was applied by comparing training data labels with network outputs to compute errors. Leveraging this error information, a gradient descent algorithm was employed to adjust the weights and bias terms of the DBN. The purpose of this adjustment is to achieve optimal parameters based on the current dataset and network model. Throughout the two stages of training, namely greedy pre-training and comprehensive fine-tuning, the DBN has developed the capability to learn high-level feature representations of data distributions while capturing intricate relationships between errors and influencing factors. It should be emphasized that hyperparameter settings, such as the number of neurons in the hidden layer and the learning rate, have a significant impact on the accuracy of DBN model predictions. Deviations from these hyperparameter settings during training can result in the model converging to a local optimum.

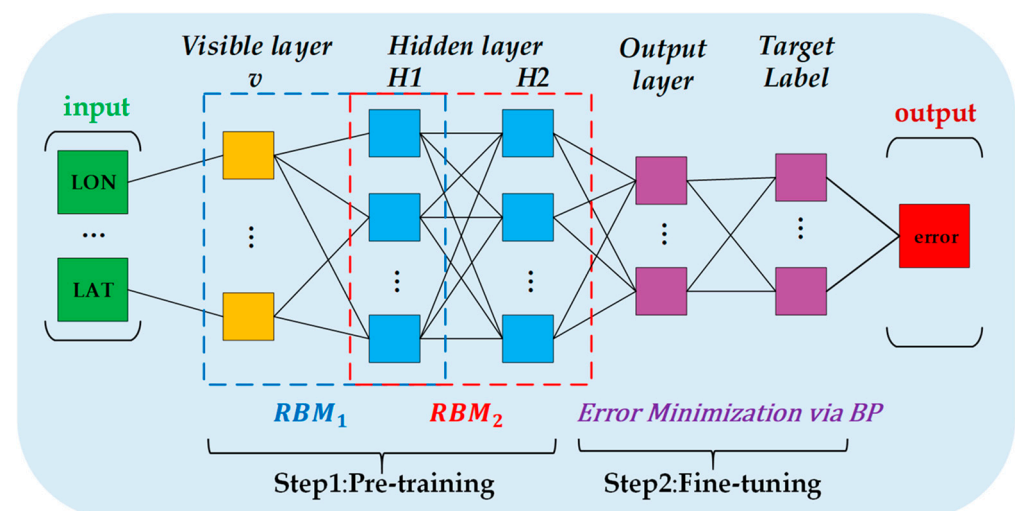


**Figure 2.** The overall structure of DBN with two RBMs.

Hence, in this study, we utilized a PSO intelligent algorithm to determine the optimal combination of hyperparameter. PSO draws inspiration from the collective behavior of birds and leverages synergy between particles and a stochastic search to efficiently explore global optimal solutions. Prior to training the DBN, we establish the search space and define the parameters for PSO. Initially, PSO initializes a group of particles within the feasible solution space, where each particle represents a potential solution point for extreme value

optimization. Three key attributes characterize each particle: position, velocity, and fitness value. The positions of particles correspond to optimized hyperparameter values that are initially randomized. The fitness function chosen for evaluating model performance is the root mean square error (RMSE), which is computed using Equation (1) to calculate the fitness value associated with each particle's position. This fitness value represents the RMSE of the DBN model's prediction result, which is based on current number of hidden layer nodes and learning rate. The fitness value of each particle  $F_{\text{fitness}}$  is compared with its individual extreme value  $P_{\text{best}}$ . If the current fitness value of a particle  $F_{\text{fitness}}$  is smaller than its individual extreme value  $P_{\text{best}}$ , the latter is updated to match the former; otherwise, it remains unchanged. Subsequently, all individual extreme values  $P_{\text{best}}$  across the particle swarm are compared to determine the population's best extreme value  $G_{\text{best}}$ . If an individual extreme value  $P_{\text{best}}$  is smaller than the population's extreme value  $G_{\text{best}}$ , it replaces the latter; otherwise, no changes are made.

$$F_{\text{fitness}} = \sqrt{\frac{1}{n} \sum_{i=1}^n (p - q)^2} \quad (1)$$

where  $n$  represents the total number of samples,  $p$  and  $q$  represent the elevation error prediction values of the DBN model under the current hyperparameters and true elevation error values, respectively.

In each iteration, the particles are meticulously tracked by maintaining records of both individual extremes  $P_{\text{best}}$  and population extremes  $G_{\text{best}}$ . These records play a crucial role in updating the individual velocity and position, subsequently leading to the continuous refinement of the hyperparameters of the DBN model. With each position update, the particle computes its fitness value and compares it to the fitness values associated with  $P_{\text{best}}$  (individual extreme value), the  $G_{\text{best}}$  (population extreme value), and the positions of population extremes. This process yields the global optimal solution for the problem [45]. The equations governing the update of particle velocity and position are presented in Equations (2) and (3):

$$V_{\text{im}}^{t+1} = \omega V_{\text{im}}^t + c_1 r_1 (P_{\text{im}}^t - X_{\text{im}}^t) + c_2 r_2 (G_m^t - X_{\text{im}}^t) \quad (2)$$

$$X_{\text{im}}^{t+1} = X_{\text{im}}^t + V_{\text{im}}^{t+1} \quad (3)$$

Among these variables,  $\omega$  represents the inertial weight of particles, which is utilized to regulate the search range in the solution space.  $c_1$  and  $c_2$  are learning factors employed for adjusting the learning rate.  $r_1$  and  $r_2$  are random numbers with values ranging from 0 to 1.  $i$  denotes the  $i$ th particle,  $m$  signifies the dimensionality of the variables, and  $t$  stands for the iteration count.  $V_{\text{im}}^t$  denotes the velocity of particle  $i$  in the  $m$ th dimension during the  $t$ th iteration.  $P_{\text{im}}^t$  represents the coordinate of particle  $i$ 's individual best value found in the  $m$ th dimension during the  $t$ th iteration.  $G_m^t$  signifies the position of the global optimum solution discovered by all particles within their swarm in the  $m$ th dimension during the  $t$ th iteration.

The iteration process concludes upon reaching the predefined maximum number of iterations. At this point, the population's extreme value, denoted as  $G_{\text{best}}$ , is identified to represent the optimal combination of learning rate and the number of neurons. Subsequently, the DBN model undergoes training using these optimized hyperparameters. Throughout the training phase, an evaluation of the model's performance is conducted through a 10-fold cross-validation methodology. Particularly, the training dataset is randomly divided into ten equally sized subsets. Among these subsets, one serves as the validation set while the remaining nine collectively form the training set. Importantly, each subset assumes both roles of training and test data across all tenfold cross-validation iterations. The training set in each instance of the 10-fold cross-validation is utilized for model training while the test set assesses its outcomes.

In this study, we selected the SRTM DEM of the Chenzhou and Yongzhou forest regions as our representative dataset for error prediction and analysis. The training set data for each experimental areas was used separately. To predict errors, we employed the methodology illustrated in Figure 3 to determine optimal parameters for the PSO-DBN model. Specifically, we set a search range of [20, 120] neurons within two hidden layers while exploring learning rates between [0.001, 0.1]. Our particle swarm consisted of 20 particles with a maximum iteration cap at 50. We then derived the corrected SRTM DEM elevation data by subtracting predicted error values from the original SRTM DEM elevation data using the PSO-DBN model; this corrected dataset represents an improved version of the SRTM DEM elevation data.

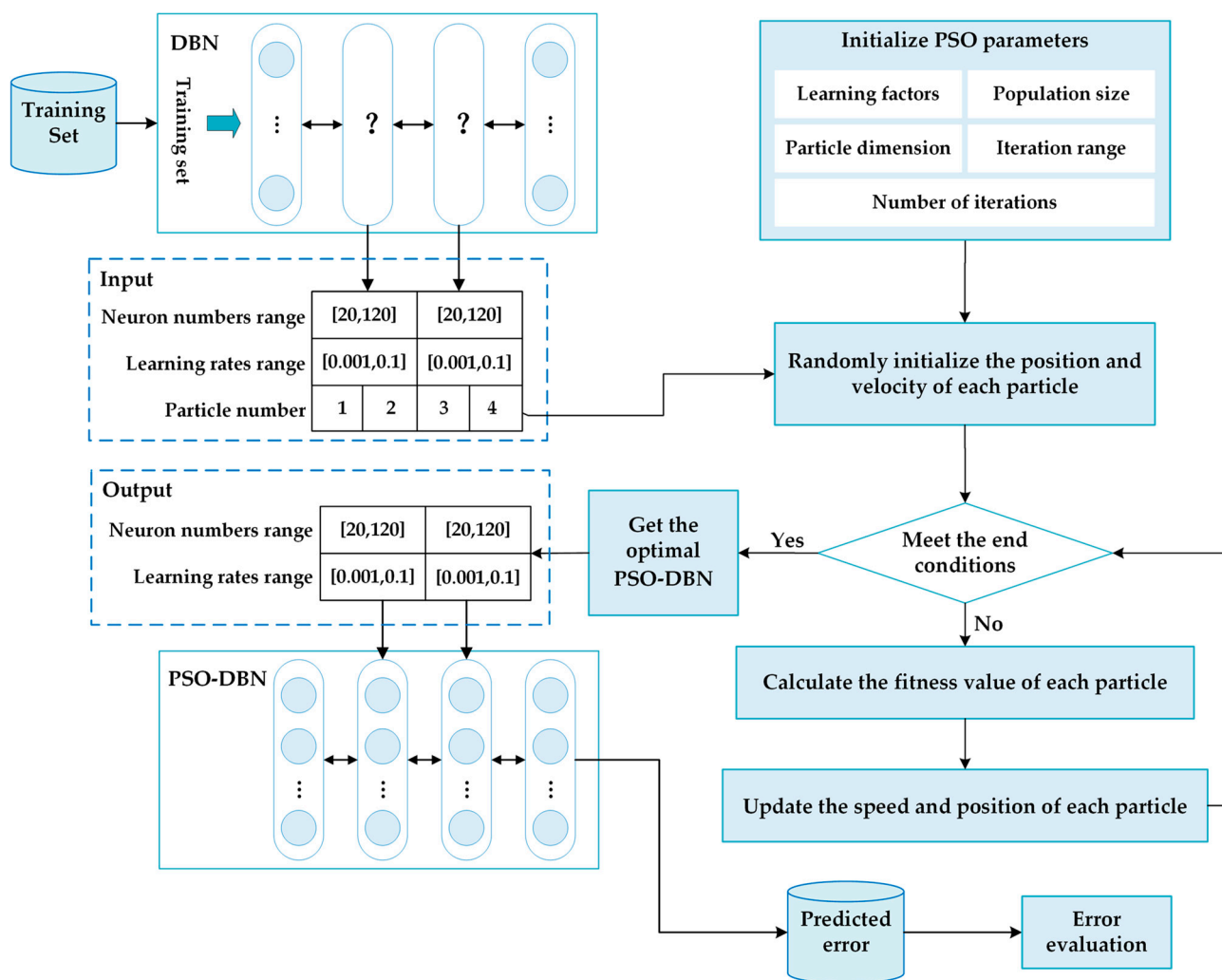


Figure 3. SRTM DEM error correction model based on particle swarm optimized deep confidence network.

After the completion of error correction for the SRTM DEM, an assessment was conducted to determine its accuracy using mean error (ME) and root mean square error (RMSE) [45], Equations (4) and (5) represent the formulas for ME and RMSE, respectively:

$$ME = \frac{1}{n} \sum_{i=1}^n h_{i,SRTM} - h_{i,icesat} \quad (4)$$

$$RMSE = \sqrt{\frac{1}{n} \sum_{i=1}^n (h_{i,SRTM} - h_{i,icesat})^2} \quad (5)$$



Equations (4) and (5) involve the elevation values of the corrected SRTM DEM product, represented by  $h_{i,SRTM}$ , the corresponding elevation control data denoted by  $h_{i,icesat}$ , and  $n$  indicating the total count of elevation control points.

## 4. Results and Discussion

### 4.1. Overall Accuracy

The error histograms in Figure 4 illustrate the disparities between the Original SRTM DEM and the PSO-DBN Corrected SRTM DEM when compared to the ICESat-2 reference elevation data. Particularly, Figure 4a provides insight into the performance metrics for Chenzhou, where we observe ME of 4.01 m and RMSE of 11.20 m for the Original SRTM DEM. The metrics for Yongzhou, as shown in Figure 4b, reveal that the Original SRTM DEM has ME of 2.31 m and RMSE of 10.29 m. It is worth noting that both Chenzhou and Yongzhou exhibit positive ME values, indicating a consistent overestimation of elevation values by the SRTM DEMs when compared to the ICESat-2 reference elevation data. This phenomenon, which is widespread in the eastern Tibetan Plateau of China [46], Jiangxi Province, China [39], and the Pearl River Delta region [47], is primarily attributed to the limited penetration capabilities of the SRTM radar center. The obstructing vegetation canopies prevent it from reaching the ground level, resulting in incomplete data acquisition [48,49]. Furthermore, it is observed that the ME and RMSE values for Chenzhou exhibit a significant increase of 42.4% and 8.1%, respectively, compared to those for Yongzhou. The observed discrepancy can be attributed to the increased topographical complexity and a broader elevation range within Chenzhou, which is characterized by a mean slope of  $15.3^\circ$ , in comparison to Yongzhou with a mean slope of  $15.7^\circ$ . Additionally, Chenzhou exhibits a higher vegetation density (67.7% vegetation cover) compared to Yongzhou (61.9% vegetation cover), which consequently leads to a lower accuracy of the raw SRTM DEM dataset of Chenzhou in comparison to that of Yongzhou.

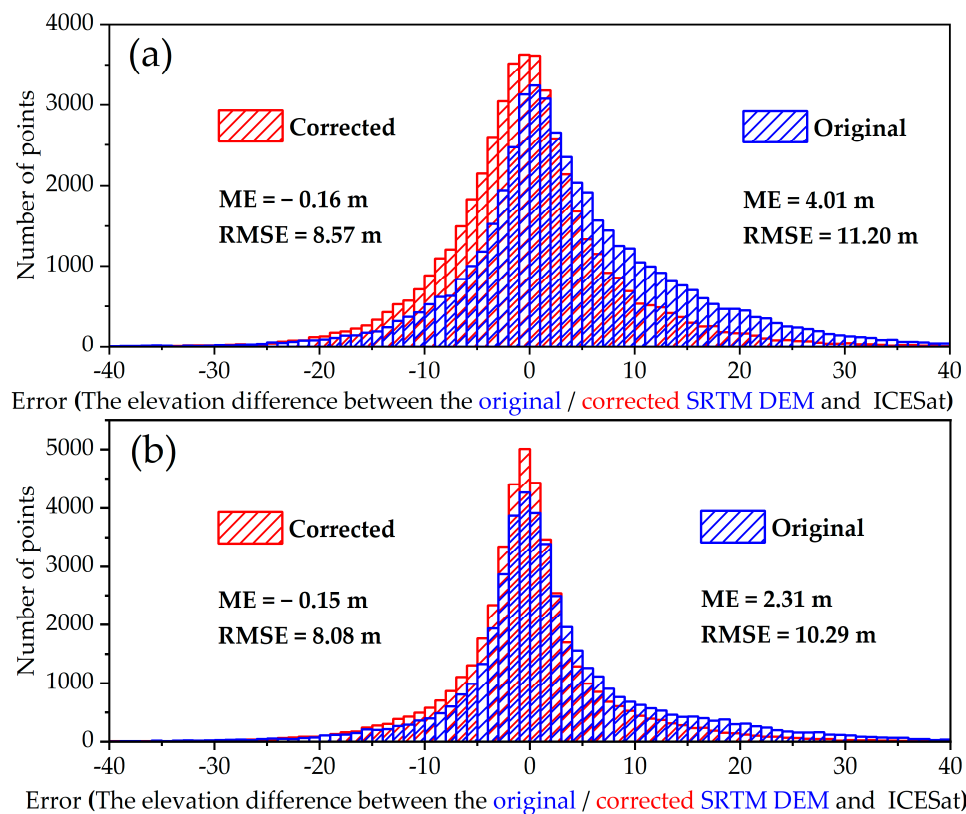


**Figure 4.** Error histograms of SRTM3 DEM relative to ICESat/GLAS data before and after PSO-DBN correction for (a) Chenzhou and (b) Yongzhou.

The PSO-DBN algorithm, introduced in this study, has demonstrated a significant capacity to enhance the accuracy of the initial SRTM DEMs within the Chenzhou and Yongzhou regions. Specifically, the application of PSO-DBN has resulted in a remarkable reduction in ME from 4.01 m to  $-0.16$  m in Chenzhou and from 2.31 m to 0.15 m in Yongzhou. ME in both areas has been eliminated by more than 93.5%. Additionally, the RMSE for Chenzhou has been reduced from 11.20 m to 8.57 m, indicating a significant decrease of 23.5%. Similarly, Yongzhou has witnessed a reduction in its RMSE from 10.29 m to 8.08 m, representing a notable decline of 21.5%. It is worth noting that the slight underestimation observed in the corrected SRTM DEM elevation values across all regions is indeed justifiable and reasonable. In fact, this phenomenon aligns with the inherent characteristics of signals obtained from ICESat-2's sensors, which are susceptible to attenuation caused by reflections from scatterers within the vegetation canopy. Consequently, it is not unexpected for some degree of overestimation to be observed in the acquired elevation values [50].

Figure 5a,d depict the original SRTM DEMs of Yongzhou and Chenzhou, respectively, and Figure 5b,e display the corrected SRTM DEMs by using the PSO-DBN algorithm in Yongzhou and Chenzhou regions, respectively. While Figure 5c,f show the elevation differences between the corrected SRTM DEMs and the original SRTM DEMs. The results indicate that the corrected SRTM DEMs using PSO-DBN algorithm are generally lower than the original SRTM DEMs, with differences primarily concentrated in the range of  $-10$  to 50 m. From Figure 5c,f, it is evident that the PSO-DBN algorithm significantly enhances the accuracy of SRTM DEM in rugged terrain and dense vegetation. However, grid differences before and after correction in the study areas span a range of  $-261$  to 257 m, with certain pixels exhibiting differences exceeding 200 m. This is attributed to data voids in the original SRTM DEMs in these locations, which were filled by the PSO-DBN algorithm, leading to the occurrence of outliers [51].

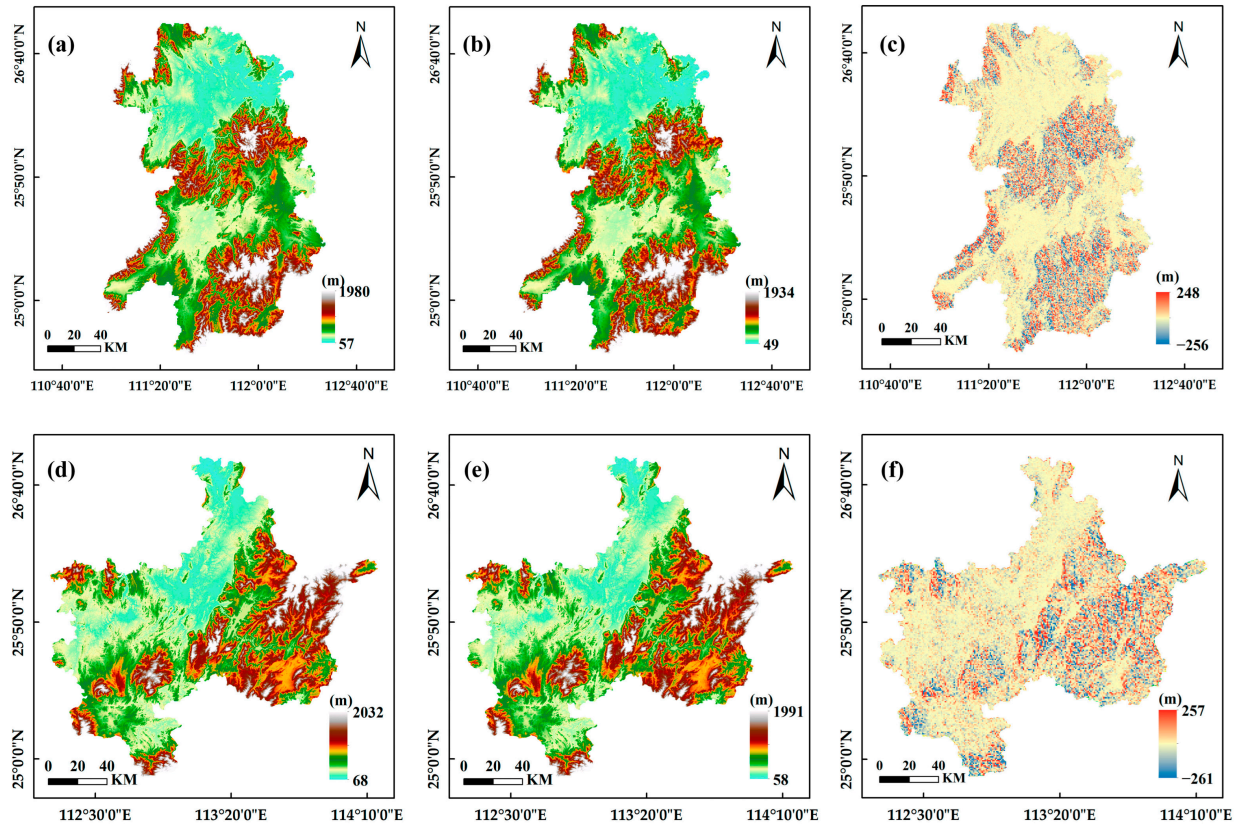


**Figure 5.** Original SRTM DEMs (a,d) of Yongzhou and Chenzhou. Corrected SRTM DEMs (b,e) by using PSO-DBN algorithm in Yongzhou and Chenzhou regions. The difference (c,f) between the original SRTM DEMs and the corrected SRTM DEMs.

#### 4.2. The Influence of Different Terrain Factors on Error Prediction of SRTM3 DEM

The accuracy of the original SRTM DEM compared to the DBN and PSO-DBN corrected SRTM DEM is depicted in Figure 6, with a specific focus on varying elevations and slopes within the forested area. In Figure 6a and Table 2, it becomes apparent that the ME of the original SRTM DEM exhibit an escalation from 0.26 m to 6.76 m, while the RMSE increases from 4.48 m to 19.80 m as slope steepness rises. This phenomenon occurs as a result of the presence of steeper slopes, which can cause foreshortening. Foreshortening refers to a situation where the difference in slant distance covered by the radar beam from the top to the bottom of a sloped surface is smaller compared to that of an equivalent ground surface. Consequently, the slant distance depicted in the image appears shorter than the actual ground surface length. This, in turn, results in a distortion of the length of the slope within the image [52]. Figure 6b and Table 2 further reveal that without correction, there is an increase in the ME from 1.59 m to 5.18 m for the SRTM DEM data, and the RMSE escalates from 5.25 m to 14.05 m as elevation rises. This can be attributed to regions with elevated terrain often exhibiting complex topography and substantial slopes, which subsequently contribute to an increase in error magnitude as elevation increases [39]. Remarkably, as illustrated in Figure 6b, the error within the forested area between 450 m to 600 m above sea level closely mirrors that observed in regions surpassing an elevation of 600 m. This implies that the impact of elevation on the error tends to stabilize at elevations exceeding 450 m above sea level, contrasting with regions below this threshold. Such behavior is likely attributed to the intricate interplay of terrain characteristics, land use patterns, and forest canopy factors, all of which collectively influence the accuracy of the SRTM DEM [39,41,53,54].

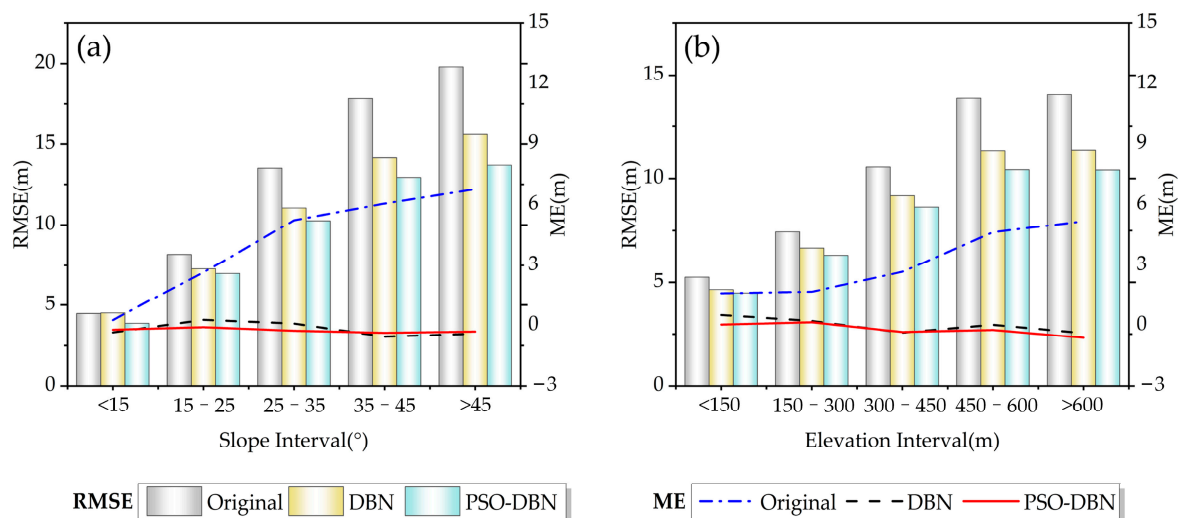


**Figure 6.** Distribution of errors in the original SRTM DEM and corrected SRTM DEM using DBN, and PSO-DBN methods for different (a) slopes and (b) elevations in the study area.

The accuracy of the original SRTM DEM, the DBN-Corrected SRTM DEM, and the PSO-DBN Corrected SRTM DEM across various elevation and slope intervals is comprehensively presented in Table 2. Importantly, Table 2 highlights the significant improvements achieved by the DBN and PSO-DBN methods in enhancing the vertical accuracy of the original SRTM DEM within different elevation intervals. After applying PSO-DBN correction, the RMSE values for the original SRTM DEM, which initially ranged from 5.25 m to 14.05 m, exhibited a significant reduction in the range of 4.47 m to 10.41 m. This notable enhancement in RMSE surpasses the corrective impact achieved by DBN (ranging from 4.64 m to 11.38 m). The PSO-DBN correction method specifically leads to a remarkable improvement in accuracy, with an enhancement of 14.8%, 15.0%, 18.2%, 24.9%, and 25.9% observed across five elevation interval ranges spanning from low to high elevations. Ad-

ditionally, significant reductions in RMSE are observed within all elevation ranges. In regions characterized by elevations below 150 m, typically indicating flat terrains, the DBN-corrected RMSE experiences a decrease of 11.6%, while PSO-DBN achieves a more substantial reduction of 14.8%. The PSO-DBN corrected SRTM DEM demonstrates an average RMSE of 8.46 m within the low hilly terrain, ranging from elevations of 150 m to 600 m, surpassing DBN's RMSE of 9.06 m. In the plateau areas with elevations exceeding 600 m, the accuracy improvement achieved by PSO-DBN exceeds that of DBN by 6.9%.

**Table 2.** Error distribution of the original SRTM DEM and the DBN- and PSO-DBN-corrected SRTM DEM for different elevation and slope intervals.

Terrain Actors	Classes	Original		DBN Corrected		PSO-DBN Corrected	
		ME (m)	RMSE (m)	ME (m)	RMSE (m)	ME (m)	RMSE (m)
Height (m)	<150	1.59	5.25	0.51	4.64	0.04	4.47
	150–300	1.67	7.43	0.22	6.66	0.15	6.32
	300–450	2.68	10.55	−0.36	9.17	−0.33	8.63
	450–600	4.64	13.88	0.03	11.35	−0.23	10.42
	>600	5.18	14.05	−0.38	11.38	−0.62	10.41
Slope (°)	<15	0.26	4.48	−0.35	4.51	−0.22	3.88
	15–25	2.65	8.17	0.27	7.28	−0.09	6.99
	25–35	5.23	13.49	0.09	11.04	−0.27	10.25
	35–45	6.05	17.82	−0.56	14.12	−0.37	12.91
	>45	6.76	19.80	−0.41	15.59	−0.31	13.67

The correction outcomes for various slope classes exhibit characteristics similar to those observed in different elevation ranges. Initially, the RMSE values for the experimental area ranged from 4.48 m to 19.80 m. However, after applying the PSO-DBN correction method, the RMSE values were significantly reduced to a range of 3.88 m to 13.67 m, surpassing the performance of the DBN correction (which ranged from 4.51 m to 15.59 m). Specifically, PSO-DBN correction achieved a significant improvement in accuracy by 13.4%, 14.5%, 24.0%, 27.5%, and 31.0% across five slope intervals ranging from minor to steep slopes. In areas with gentle slopes, defined as slopes less than 15°, the PSO-DBN correction method exhibits a 14.2% increase in accuracy improvement (RMSE of 3.88 m) compared to DBN correction (RMSE of 4.51 m). For sloping terrain ranging from 15° to 35°, the average RMSE values for the PSO-DBN and DBN-corrected SRTM DEMs are measured at 8.62 m and 9.16 m, respectively. When dealing with steep slopes exceeding angles greater than 35°, the PSO-DBN correction method outperforms DBN by achieving a minimum accuracy improvement of 27.5%, in contrast to the lesser improvement realized by DBN at only 20.8%.

With increasing elevation and slope values, both the PSO-DBN and DBN algorithms exhibit a consistent trend of enhancing their performance across all intervals. Notably, the PSO-DBN algorithm consistently outperforms DBN in all slope and elevation intervals due to its inherent capability to facilitate adaptive feature extraction and generalize its applications more effectively across diverse datasets.

#### 4.3. The Influence of Different Land Cover Types on SRTM DEM Error Correction

The original error metrics, including ME and RMSE, for various land cover types in the two study regions are presented in Table 3. In addition, the table showcases the error reductions achieved through the implementation of DBN and PSO-DBN algorithms. Table 3 highlights significant variations in the accuracy of raw SRTM DEMs across five distinct land cover types: cropland, forest, grassland, water bodies, and built-up land. Notably, vegetated areas such as forests and grasslands, exhibit considerably higher ME and RMSE values for raw SRTM DEM (ME: 4.03 m, RMSE: 11.32 m) compared to non-vegetated areas (ME: 0.72 m, RMSE: 6.53 m). The observed disparity arises due to the limited penetration ability of the SRTM C-band radar in forest canopies, resulting in irregular backward scattering of



radar signals that amplify geometric distortions [53,54]. Additionally, temporal variations in data acquisition between SRTM and ICESat, which correspond to different surface conditions, including vegetation, contribute to these discrepancies [53]. Table 3 presents compelling evidence that both the DBN and PSO-DBN methodologies effectively mitigate the ME across vegetated and non-vegetated areas, resulting in a significant reduction of 22.0%. However, there is a noticeable disparity in their efficacy in reducing the RMSE. For areas with vegetated cover, DBN and PSO-DBN achieved a reduction of 17.5% (from 11.32 m to 9.34 m) and 20.6% (to 8.99 m), respectively, for the SRTM DEM dataset. In forests, the reductions were 17.6% and 22.2%, while in grasslands, they were 17.6% and 18.3%. This discrepancy arises due to the initial higher RMSE value in forests (13.13 m) compared to grasslands (9.50 m), allowing for better error characteristic learning through a more extensive training sample dataset. In non-vegetated areas, both DBN and PSO-DBN demonstrated a reduction the RMSE from the original value of 6.53 m to 6.32 m (a decrease of 3.2%) and 5.66 m (a decrease of 13.3%), respectively. This pattern of improvement extends to specific land cover types as well: for water bodies, the RMSE decreased from 8.59 m to 7.68 m (a reduction of 10.6%) with DBN and further decreased to 7.25 m (a reduction of 15.5%) with PSO-DBN; for cropland, the RMSE decreased from 5.21 m to 4.72 m (a decrease of 9.4%) using DBN and further reduce to 4.48 m (a decrease of 14.0%), respectively; similarly, for man-made surfaces, the RMSE decreased from its original value of 5.79 m to 5.65 m (a reduction of 2.4%) with DBN and further decrease to 5.25 m (a reduction of 9.3%) with PSO-DBN.

**Table 3.** ME and RMSE before and after SRTM DEM correction for different surface cover types.

Land Cover Type	Number of Test Observations	Original		DBN Corrected		PSO-DBN Corrected	
		ME (m)	RMSE (m)	ME (m)	RMSE (m)	ME (m)	RMSE (m)
cultivated land	8464	0.75	5.21	−0.39	4.72	−0.26	4.48
forestland	15873	4.58	13.13	0.22	10.85	−0.13	10.21
grassland	2802	3.47	9.50	0.09	7.83	−0.55	7.76
water area	488	0.45	8.59	−1.80	7.68	−0.80	7.25
built-up land	541	0.95	5.79	−0.74	5.65	0.79	5.25

The results confirm that PSO-DBN significantly enhances the accuracy of SRTM DEMs across various land cover types, thereby demonstrating the robustness of the model. Importantly, PSO-DBN achieves a 3.1% and 10.1% greater improvement in accuracy compared to DBN in vegetated and non-vegetated areas, respectively.

#### 4.4. The Influence of Different Vegetation Types on SRTM DEM Error Correction

The study area predominantly falls within the subtropical monsoon humid climate category, characterized by significant vertical variations due to its mountainous terrain. A distinct pattern of vertical vegetation differentiation exists, with prevalent vegetation types including Evergreen Needle-leaved Forests, Deciduous Broadleaved Forests, and Evergreen Broadleaved Forests. The results of SRTM DEM correction for Evergreen Needle-leaved Forests, Deciduous Broadleaved Forests, and Evergreen Broadleaved Forests using the DBN and PSO-DBN algorithms are illustrated in Figure 6. The ME and RMSE of the SRTM DEM exhibit a strong correlation with forest type, as illustrated in Figure 6. Notably, Evergreen Broadleaved Forests demonstrate the highest ME and RMSE measurements of 5.77 m and 14.31 m correspondingly. In contrast, Deciduous Broadleaved Forests closely follow with ME and RMSE values of 5.20 m and 14.07 m. In contrast, Evergreen Coniferous Forests exhibits the lowest error rates, with a ME of 1.18 m and a RMSE of 11.94 m. It is precisely because, Evergreen Broadleaved Forests typically boast the highest average tree height and present challenges for radar signal penetration due to their canopy and foliage characteristics [27]. In the case of Deciduous Broadleaved Forests, lower ME and RMSE values can be responsible for the timing of SRTM DEM acquisition during the

deciduous stage, reduced canopy coverage [31], as well as decreased air moisture content and relatively cooler air temperatures during this period. Radar signals tend to penetrate deeper under dry or freezing conditions compared to warm or humid conditions due to the lower liquid water content and dielectric constant within the forest canopy [50,53]. Interestingly, Evergreen Broadleaved Forests demonstrate minimal errors, indicating their superior SAR microwave penetration capabilities within this vegetation cover. Several factors, such as vegetation density, polarization, tree structure, effective baseline, angle of incidence, and weather conditions, may influence the depth of SAR microwave penetration into vegetation [35,55].

The results presented in Figure 7 demonstrate the effective reduction in ME achieved by both the DBN and PSO-DBN algorithms in various forested regions, with a substantial decrease of over 91.2%. However, it is noteworthy that PSO-DBN outperforms DBN significantly in terms of reducing the RMSE. Specifically, in Deciduous Broadleaved Forests, PSO-DBN and DBN reduce the RMSE from 14.07 m to 10.39 m (26.2% reduction) and 12.26 m (12.9% reduction), respectively. For Evergreen Broadleaved Forests, PSO-DBN and DBN decrease the RMSE from 14.31 m to 10.56 m (26.2% reduction) and 11.79 m (17.6% reduction), respectively. In the Evergreen Needle-leaved Forest zone, PSO-DBN and DBN achieve a reduction in RMSE from 11.94 m to 10.17 m (14.8% reduction) and 11.25 m (5.8% reduction), respectively. The variation in accuracy improvement among the three vegetation zones may be attributed to the initial accuracy levels of the respective vegetation cover types and the availability of training sample points. In areas with nearly identical vegetation cover within the same study region, PSO-DBN corrected SRTM DEM consistently exhibits smaller errors than DBN-corrected SRTM DEM. On average, PSO-DBN achieves approximately 10% higher corrected accuracy compared to DBN.

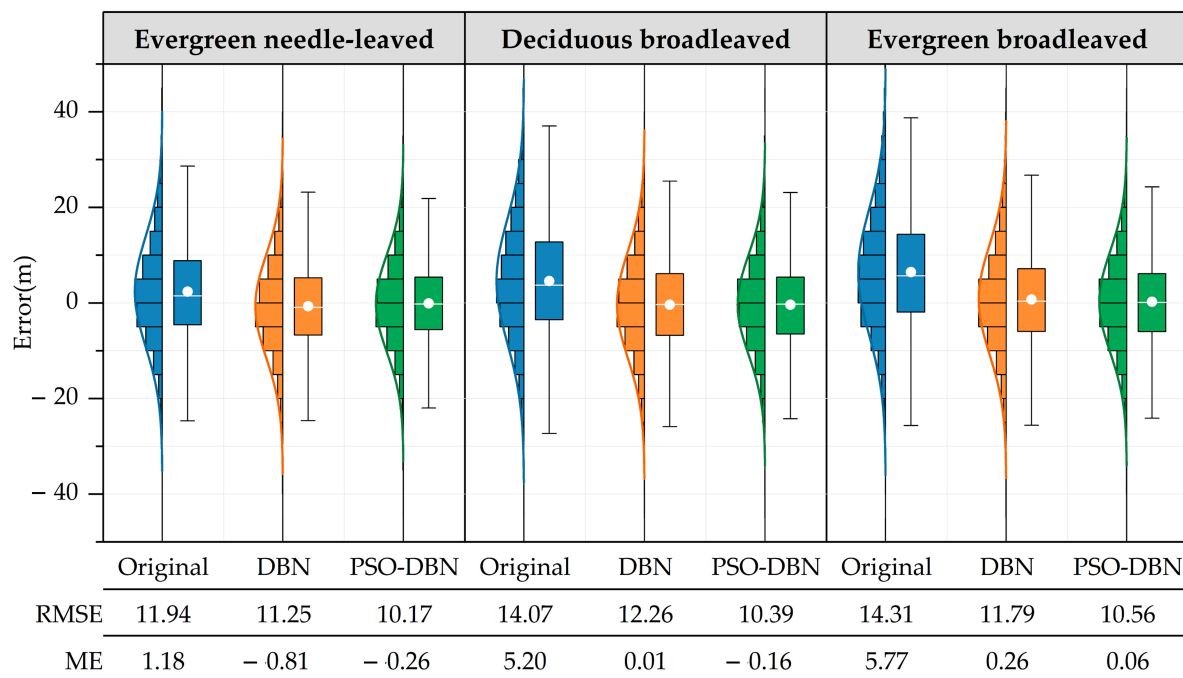


**Figure 7.** SRTM of Evergreen Needle-leaved Forest, Deciduous Broadleaved Forest, and Evergreen Broadleaved Forest areas corrected by DBN and PSO-DBN methods. The segmented bar chart represents the distribution of data, the normal curve fits the trend of data distribution. The central horizontal line within the box represents the median. The box displays the interquartile range (25th to the 75th percentile), and the whiskers indicate 1.5 times the interquartile range.

#### 4.5. Model Performance Comparison

In order to evaluate the efficacy of the Deep Belief Network (DBN) and Particle Swarm Optimization-Deep Belief Network (PSO-DBN) algorithms, we employed traditional Multivariate Linear Regression (MLR), Multivariate Nonlinear Regression (MNLN), and Artificial Neural Network (ANN) models for comparative analysis. The error correction effects of the five algorithms on SRTM DEM are presented in Table 4.

**Table 4.** Accuracy comparison of SRTM DEMs corrected by PSO-DBN, DBN, MLR, MNLN and ANN algorithms.

Models	ME (m)		RMSE (m)	
	Original	Corrected	Original	Corrected
MLR	4.01	3.72	10.46	10.43
MNLN	4.01	0.10	10.46	10.19
ANN	3.13	0.18	11.12	8.87
DBN	3.98	−0.06	11.07	9.20
PSO-DBN	3.16	−0.16	10.75	8.33

As can be seen from Table 4, the accuracies of SRTM DEMs corrected by PSO-DBN, DBN, MLR, MNLN and ANN algorithms are improved. The accuracies of MLR and MNLN are only increased by 0.3% and 2.6%, respectively, while the results corrected by ANN, DBN and PSO-DBN show better performance, and the accuracies are increased by 20.2%, 16.9%, and 22.5%, respectively. In comparison to the other four algorithms, the PSO-DBN algorithm proposed in this paper has obvious advantages in SRTM DEM correction. Specifically, compared with MLR, MNLN, ANN, and DBN, the accuracies of SRTM DEM corrected by the PSO-DBN algorithm are improved by 22.2%, 19.9%, 2.3%, and 5.6%, respectively. This is attributed to the PSO-DBN algorithm can better capture the complex relationship between errors and influencing factors compared to regression methods. Additionally, particle swarm optimization is used to optimize the hyperparameters of DBN, which effectively avoids the overfitting problem common in classical machine learning methods.

#### 5. Conclusions

The present study proposes a method for correcting SRTM DEM errors by employing deep confidence networks optimized through the PSO algorithm. This approach takes into consideration various factors that influence terrain and vegetation parameters. To validate our methodology, we selected two study areas, Chenzhou and Yongzhou in Hunan Province, China, which are characterized by complex terrain and high vegetation coverage. Our experimental findings reveal the following key observations: (1) Among terrain-related factors, both slope and elevation exhibit a positive correlation with errors in the SRTM DEM. It is important that, both PSO-DBN and DBN demonstrate superior performance in correcting the SRTM DEM in regions with complex terrain. Specifically, when the slope exceeds 35°, the accuracy of SRTM DEMs corrected by PSO-DBN exhibits an improvement of 34.5% (Chenzhou) and 25.3% (Yongzhou), while DBN correction results in an enhancement of 20.3% and 18.0%, respectively. Furthermore, at elevations exceeding 600 m, the accuracy of SRTM DEMs corrected by PSO-DBN shows an increase of 26.4% (Chenzhou) and 25.2% (Yongzhou), with DBN correction resulting in improvements of 19.1% and 18.9%, respectively. (2) Additionally, the application of PSO-DBN correction in vegetated regions leads to a reduction in RMSE of over 20%. Across different forest types, PSO-DBN's error correction performance clearly surpasses that of DBN. In broadleaf forest areas, the accuracy of SRTM DEMs corrected by PSO-DBN increases by 26.9% (Chenzhou) and 25.3% (Yongzhou), while DBN achieves improvements of 20.1% and 19.2%, respectively. In coniferous forest areas, PSO-DBN results in enhancements of 15.8% (Chenzhou) and 13.1% (Yongzhou), while DBN exhibits improvements of 11.7% and 7.1%, respectively.

Overall, the ME of SRTM DEM corrected by both DBN and PSO-DBN experiences a reduction of over 90% in the experimental areas, with average RMSE decreasing by 16.4% and 22.5%, respectively. Notably, regardless of varying topographical conditions, land cover types, and vegetation characteristics encountered, PSO-DBN consistently outperforms DBN.

Additionally, our study has identified instances of missing ICESat-2 data in certain areas, which may potentially impact the overall calibration of the SRTM DEM. Furthermore, regions characterized by high vegetation cover, dense canopy, and complex vertical forest structures can introduce errors in the ICESat-2 elevation control data itself. Consequently, future research endeavors will obtain reference data with more uniformly distributed or higher accuracy to correct SRTM DEM, such as airborne LiDAR DEM data.

**Author Contributions:** Conceptualization, X.S. and C.Z.; funding acquisition, C.Z.; methodology, X.S., C.Z., J.X. and Z.O.; resources, C.Z., J.X. and Y.L.; supervision, C.Z., J.X. and Y.L.; writing—original draft, X.S.; writing—review and editing, X.S., C.Z., Z.O. and Y.L. All authors have read and agreed to the published version of the manuscript.

**Funding:** This research was funded by the National Natural Science Foundation of China (No. 42074016 and 42030112) and the Hunan Provincial Natural Science Foundation of China (No. 2021JJ30244).

**Acknowledgments:** Many thanks to NASA and USGS for providing free datasets.

**Conflicts of Interest:** The authors declare no conflict of interest.

## References

1. Li, H.; Zhao, J. Evaluation of the Newly Released Worldwide AW3D30 DEM Over Typical Landforms of China Using Two Global DEMs and ICESat/GLAS Data. *IEEE J. Sel. Top. Appl. Earth Obs. Remote Sens.* **2018**, *11*, 4430–4440. [[CrossRef](#)]
2. Parizi, E.; Khojeh, S.; Hosseini, S.M.; Moghadam, Y.J. Application of Unmanned Aerial Vehicle DEM in Flood Modeling and Comparison with Global DEMs: Case Study of Atrak River Basin, Iran. *J. Environ. Manag.* **2022**, *317*, 115492. [[CrossRef](#)] [[PubMed](#)]
3. Zhang, N.; Chen, M.; Yang, F.; Yang, C.; Yang, P.; Gao, Y.; Shang, Y.; Peng, D. Forest Height Mapping Using Feature Selection and Machine Learning by Integrating Multi-Source Satellite Data in Baoding City, North China. *Remote Sens.* **2022**, *14*, 4434. [[CrossRef](#)]
4. Li, J.; Wang, W.; Chen, G.; Han, Z. Spatiotemporal Assessment of Landslide Susceptibility in Southern Sichuan, China Using SA-DBN, PSO-DBN and SSA-DBN Models Compared with DBN Model. *Adv. Space Res.* **2022**, *69*, 3071–3087. [[CrossRef](#)]
5. Frey, H.; Paul, F. On the Suitability of the SRTM DEM and ASTER GDEM for the Compilation of Topographic Parameters in Glacier Inventories. *Int. J. Appl. Earth Obs. Geoinf.* **2012**, *18*, 480–490. [[CrossRef](#)]
6. Ngula Niipele, J.; Chen, J. The Usefulness of Alos-Palsar Dem Data for Drainage Extraction in Semi-Arid Environments in The Iishana Sub-Basin. *J. Hydrol. Reg. Stud.* **2019**, *21*, 57–67. [[CrossRef](#)]
7. Mukul, M.; Srivastava, V.; Mukul, M. Accuracy Analysis of the 2014–2015 Global Shuttle Radar Topography Mission (SRTM) 1 Arc-Sec C-Band Height Model Using International Global Navigation Satellite System Service (IGS) Network. *J. Earth Syst. Sci.* **2016**, *125*, 909–917. [[CrossRef](#)]
8. Mukherjee, S.; Joshi, P.K.; Mukherjee, S.; Ghosh, A.; Garg, R.D.; Mukhopadhyay, A. Evaluation of Vertical Accuracy of Open Source Digital Elevation Model (DEM). *Int. J. Appl. Earth Obs. Geoinf.* **2013**, *21*, 205–217. [[CrossRef](#)]
9. Gruber, A.; Wessel, B.; Huber, M.; Roth, A. Operational TanDEM-X DEM Calibration and First Validation Results. *ISPRS J. Photogramm. Remote Sens.* **2012**, *73*, 39–49. [[CrossRef](#)]
10. Cenci, L.; Galli, M.; Palumbo, G.; Sapia, L.; Santella, C.; Albinet, C. Describing the Quality Assessment Workflow Designed for DEM Products Distributed Via the Copernicus Programme. Case Study: The Absolute Vertical Accuracy of the Copernicus DEM Dataset in Spain. In Proceedings of the 2021 IEEE International Geoscience and Remote Sensing Symposium IGARSS, Brussels, Belgium, 11 July 2021; pp. 6143–6146.
11. Almeida, L.; Almar, R.; Bergsma, E.; Berthier, E.; Baptista, P.; Garel, E.; Dada, O.; Alves, B. Deriving High Spatial-Resolution Coastal Topography From Sub-Meter Satellite Stereo Imagery. *Remote Sens.* **2019**, *11*, 590. [[CrossRef](#)]
12. Su, Y.; Guo, Q.; Ma, Q.; Li, W. SRTM DEM Correction in Vegetated Mountain Areas through the Integration of Spaceborne LiDAR, Airborne LiDAR, and Optical Imagery. *Remote Sens.* **2015**, *7*, 11202–11225. [[CrossRef](#)]
13. Young, S.S.; Wamburu, P. Comparing Drone-Derived Elevation Data with Air-Borne LiDAR to Analyze Coastal Sea Level Rise at the Local Level. *Pap. Appl. Geogr.* **2021**, *7*, 331–342. [[CrossRef](#)]
14. Mancini, F.; Dubbini, M.; Gattelli, M.; Stecchi, F.; Fabbri, S.; Gabbianelli, G. Using Unmanned Aerial Vehicles (UAV) for High-Resolution Reconstruction of Topography: The Structure from Motion Approach on Coastal Environments. *Remote Sens.* **2013**, *5*, 6880–6898. [[CrossRef](#)]



15. Sun, G.; Ranson, K.; Kimes, D.; Blair, J.; Kovacs, K. Forest Vertical Structure from GLAS: An Evaluation Using LVIS and SRTM Data. *Remote Sens. Environ.* **2008**, *112*, 107–117. [[CrossRef](#)]
16. Gorokhovitch, Y.; Voustianiouk, A. Accuracy Assessment of the Processed SRTM-Based Elevation Data by CGIAR Using Field Data from USA and Thailand and Its Relation to the Terrain Characteristics. *Remote Sens. Environ.* **2006**, *104*, 409–415. [[CrossRef](#)]
17. Chen, H.; Liang, Q.; Liu, Y.; Xie, S. Hydraulic Correction Method (HCM) to Enhance the Efficiency of SRTM DEM in Flood Modeling. *J. Hydrol.* **2018**, *559*, 56–70. [[CrossRef](#)]
18. Guth, P.L.; Geoffroy, T.M. LiDAR Point Cloud and ICESat-2 Evaluation of 1 Second Global Digital Elevation Models: Copernicus Wins. *Trans. GIS* **2021**, *25*, 2245–2261. [[CrossRef](#)]
19. Li, H.; Zhao, J.; Yan, B.; Yue, L.; Wang, L. Global DEMs Vary from One to Another: An Evaluation of Newly Released Copernicus, NASA and AW3D30 DEM on Selected Terrains of China Using ICESat-2 Altimetry Data. *Int. J. Digit. Earth* **2022**, *15*, 1149–1168. [[CrossRef](#)]
20. Wendi, D.; Liang, S.-Y.; Sun, Y.; Doan, C.D. An Innovative Approach to Improve SRTM DEM Using Multispectral Imagery and Artificial Neural Network: An Innovative Approach to Improve SRTM. *J. Adv. Model. Earth Syst.* **2016**, *8*, 691–702. [[CrossRef](#)]
21. Pham, H.T.; Marshall, L.; Johnson, F.; Sharma, A. A Method for Combining SRTM DEM and ASTER GDEM2 to Improve Topography Estimation in Regions without Reference Data. *Remote Sens. Environ.* **2018**, *210*, 229–241. [[CrossRef](#)]
22. Li, Y.; Fu, H.; Zhu, J.; Wu, K.; Yang, P.; Wang, L.; Gao, S. A Method for SRTM DEM Elevation Error Correction in Forested Areas Using ICESat-2 Data and Vegetation Classification Data. *Remote Sens.* **2022**, *14*, 3380. [[CrossRef](#)]
23. Zhou, C.; Zhang, G.; Yang, Z.; Ao, M.; Liu, Z.; Zhu, J. An Adaptive Terrain-Dependent Method for SRTM DEM Correction Over Mountainous Areas. *IEEE Access* **2020**, *8*, 130878–130887. [[CrossRef](#)]
24. O’Loughlin, F.E.; Paiva, R.C.D.; Durand, M.; Alsdorf, D.E.; Bates, P.D. A Multi-Sensor Approach towards a Global Vegetation Corrected SRTM DEM Product. *Remote Sens. Environ.* **2016**, *182*, 49–59. [[CrossRef](#)]
25. Ouyang, Z.; Zhou, C.; Xie, J.; Zhu, J.; Zhang, G.; Ao, M. SRTM DEM Correction Using Ensemble Machine Learning Algorithm. *Remote Sens.* **2023**, *15*, 3946. [[CrossRef](#)]
26. Hawker, L.; Uhe, P.; Paulo, L.; Sosa, J.; Savage, J.; Sampson, C.; Neal, J. A 30 m Global Map of Elevation with Forests and Buildings Removed. *Environ. Res. Lett.* **2022**, *17*, 024016. [[CrossRef](#)]
27. Li, Y.; Li, L.; Chen, C.; Liu, Y. Correction of Global Digital Elevation Models in Forested Areas Using an Artificial Neural Network-Based Method with the Consideration of Spatial Autocorrelation. *Int. J. Digit. Earth* **2023**, *16*, 1568–1588. [[CrossRef](#)]
28. Chen, Y.; Zhao, X.; Jia, X. Spectral–Spatial Classification of Hyperspectral Data Based on Deep Belief Network. *IEEE J. Sel. Top. Appl. Earth Obs. Remote Sens.* **2015**, *8*, 2381–2392. [[CrossRef](#)]
29. Yue, L.; Shen, H.; Yuan, Q.; Liu, X. A Multi-source DEM Point-Surface Fusion Model Based on Deep Belief Network. *Geomat. Inf. Sci. Wuhan Univ.* **2021**, *46*, 1090–1097. [[CrossRef](#)]
30. Rabus, B.; Eineder, M.; Roth, A.; Bamler, R. The Shuttle Radar Topography Mission—A New Class of Digital Elevation Models Acquired by Spaceborne Radar. *Remote Sens.* **2003**, *57*, 241–262. [[CrossRef](#)]
31. Farr, T.G.; Kobrick, M. Shuttle Radar Topography Mission Produces a Wealth of Data. *Eos Trans. Am. Geophys. Union* **2000**, *81*, 583. [[CrossRef](#)]
32. Su, Y.; Guo, Q. A Practical Method for SRTM DEM Correction over Vegetated Mountain Areas. *ISPRS J. Photogramm. Remote Sens.* **2014**, *87*, 216–228. [[CrossRef](#)]
33. Neuenschwander, A.; Pitts, K. The ATL08 Land and Vegetation Product for the ICESat-2 Mission. *Remote Sens. Environ.* **2019**, *221*, 247–259. [[CrossRef](#)]
34. Schenk, T.; Csatho, B.; Neumann, T. Assessment of ICESat-2’s Horizontal Accuracy Using Precisely Surveyed Terrains in McMurdo Dry Valleys, Antarctica. *IEEE Trans. Geosci. Remote Sens.* **2022**, *60*, 4303811. [[CrossRef](#)]
35. Gdulová, K.; Marešová, J.; Moudrý, V. Accuracy Assessment of the Global TanDEM-X Digital Elevation Model in a Mountain Environment. *Remote Sens. Environ.* **2020**, *241*, 111724. [[CrossRef](#)]
36. Tian, X.; Shan, J. Comprehensive Evaluation of the ICESat-2 ATL08 Terrain Product. *IEEE Trans. Geosci. Remote Sens.* **2021**, *59*, 8195–8209. [[CrossRef](#)]
37. Satgé, F.; Bonnet, M.P.; Timouk, F.; Calmant, S.; Pillco, R.; Molina, J.; Lavado-Casimiro, W.; Arsen, A.; Crétaux, J.F.; Garnier, J. Accuracy Assessment of SRTM v4 and ASTER GDEM v2 over the Altiplano Watershed Using ICESat/GLAS Data. *Int. J. Remote Sens.* **2015**, *36*, 465–488. [[CrossRef](#)]
38. Fu, C.Y.; Tsay, J.R. Statistic Tests Aided Multi-Source DEM Fusion. *ISPRS Int. Arch. Photogramm. Remote Sens. Spat. Inf. Sci.* **2016**, *XLI-B6*, 227–233. [[CrossRef](#)]
39. Chen, C.; Yang, S.; Li, Y. Accuracy Assessment and Correction of SRTM DEM Using ICESat/GLAS Data under Data Coregistration. *Remote Sens.* **2020**, *12*, 3435. [[CrossRef](#)]
40. Zhao, X.; Su, Y.; Hu, T.; Chen, L.; Gao, S.; Wang, R.; Jin, S.; Guo, Q. A Global Corrected SRTM DEM Product for Vegetated Areas. *Remote Sens. Lett.* **2018**, *9*, 393–402. [[CrossRef](#)]
41. Magruder, L.; Neuenschwander, A.; Klotz, B. Digital Terrain Model Elevation Corrections Using Space-Based Imagery and ICESat-2 Laser Altimetry. *Remote Sens. Environ.* **2021**, *264*, 112621. [[CrossRef](#)]
42. Uuemaa, E.; Ahi, S.; Montibeller, B.; Muru, M.; Kmoch, A. Vertical Accuracy of Freely Available Global Digital Elevation Models (ASTER, AW3D30, MERIT, TanDEM-X, SRTM, and NASADEM). *Remote Sens.* **2020**, *12*, 3482. [[CrossRef](#)]

43. Kolecka, N.; Kozak, J. Assessment of the Accuracy of SRTM C- and X-Band High Mountain Elevation Data: A Case Study of the Polish Tatra Mountains. *Pure Appl. Geophys.* **2014**, *171*, 897–912. [[CrossRef](#)]
44. Cheng, R.; Jin, Y. A Social Learning Particle Swarm Optimization Algorithm for Scalable Optimization. *Inf. Sci.* **2015**, *291*, 43–60. [[CrossRef](#)]
45. Fisher, P.F.; Tate, N.J. Causes and Consequences of Error in Digital Elevation Models. *Prog. Phys. Geogr. Earth Environ.* **2006**, *30*, 467–489. [[CrossRef](#)]
46. Huang, X.; Xie, H.; Liang, T.; Yi, D. Estimating Vertical Error of SRTM and Map-Based DEMs Using ICESat Altimetry Data in the Eastern Tibetan Plateau. *Int. J. Remote Sens.* **2011**, *32*, 5177–5196. [[CrossRef](#)]
47. Du, X.; Guo, H.; Fan, X.; Zhu, J.; Yan, Z.; Zhan, Q. Vertical Accuracy Assessment of Freely Available Digital Elevation Models over Low-Lying Coastal Plains. *Int. J. Digit. Earth* **2016**, *9*, 252–271. [[CrossRef](#)]
48. Carabajal, C.C.; Harding, D.J. ICESat Validation of SRTM C-Band Digital Elevation Models: ICESat VALIDATION OF SRTM C-BAND DEMS. *Geophys. Res. Lett.* **2005**, *32*, L22S01. [[CrossRef](#)]
49. Carabajal, C.C.; Harding, D.J. SRTM C-Band and ICESat Laser Altimetry Elevation Comparisons as a Function of Tree Cover and Relief. *Photogramm. Eng. Remote Sens.* **2006**, *72*, 287–298. [[CrossRef](#)]
50. Woodhouse, I.H. Predicting Backscatter-Biomass and Height-Biomass Trends Using a Macroecology Model. *IEEE Trans. Geosci. Remote Sens.* **2006**, *44*, 871–877. [[CrossRef](#)]
51. Shen, X.; Zhou, C.; Zhu, J. Improving the Accuracy of TanDEM-X Digital Elevation Model Using Least Squares Collocation Method. *Remote Sens.* **2023**, *15*, 3695. [[CrossRef](#)]
52. Passini, R.; Jacobsen, K. Accuracy Analysis of SRTM Height Models. In Proceedings of the 2007 American Society for Photogrammetry and Remote Sensing Annual Conference, Tampa, FL, USA, 7–11 May 2007.
53. Bhang, K.J.; Schwartz, F.W.; Braun, A. Verification of the Vertical Error in C-Band SRTM DEM Using ICESat and Landsat-7, Otter Tail County, MN. *IEEE Trans. Geosci. Remote Sens.* **2007**, *45*, 36–44. [[CrossRef](#)]
54. Yu, X.; Hyypä, J.; Kaartinen, H.; Maltamo, M. Automatic Detection of Harvested Trees and Determination of Forest Growth Using Airborne Laser Scanning. *Remote Sens. Environ.* **2004**, *90*, 451–462. [[CrossRef](#)]
55. Brown, C.G.; Sarabandi, K.; Pierce, L.E. Model-Based Estimation of Forest Canopy Height in Red and Austrian Pine Stands Using Shuttle Radar Topography Mission and Ancillary Data: A Proof-of-Concept Study. *IEEE Trans. Geosci. Remote Sens.* **2010**, *48*, 1105–1118. [[CrossRef](#)]

**Disclaimer/Publisher’s Note:** The statements, opinions and data contained in all publications are solely those of the individual author(s) and contributor(s) and not of MDPI and/or the editor(s). MDPI and/or the editor(s) disclaim responsibility for any injury to people or property resulting from any ideas, methods, instructions or products referred to in the content.